Femtosecond pump–probe measurements of non-radiative relaxation in LiAlO$_2$:V^{3+}

Femtosecond pump–probe measurements of non-radiative relaxation in LiAlO$_2$:V^{3+}

Jon-Paul R Wells[1,4]**, Marek Grinberg**[2]**, Klaas Wynne**[3] **and T P J Han**[3]

[1] Department of Physics and Astronomy, University of Sheffield, Sheffield S3 7RH, UK
[2] Institute of Experimental Physics, University of Gdansk, Gdansk, PL-80952, Poland
[3] Department of Physics, University of Strathclyde, Glasgow G1 1XN, UK

E-mail: j.p.wells@sheffield.ac.uk

Abstract

We report on time-resolved studies of non-radiative relaxation of V^{3+} ions in LiAlO$_2$ by means of a two-beam, pump–probe saturation experiment performed with the 150 fs pulsed output of a Ti–sapphire laser. Exciting into the vibronically broadened ^{3}A$_2$ $\rightarrow$ ^{3}T$_1$ transition at 800 nm, a ^{3}T$_1$ relaxation time of 199 ps has been measured at 4 K. This value decreases to 82 ps at room temperature, representing a reduction in the lifetime of a factor of 2.5 due to internal-conversion processes. The relative probabilities for non-radiative, phonon-assisted barrier hopping and quantum mechanical tunnelling through the potential barrier to the ^{3}A$_2$ ground state have been obtained using Mott's expression, yielding best-fit parameters of $W_0 = (5.2 \pm 1) \times 10^9$ Hz and $W_1 = (7.5 \pm 1) \times 10^{10}$ Hz for a potential barrier of $E_{nr} = 530 \pm 50$ cm^{-1}.

1. Introduction

Crystals doped with transition-metal ions having a valence shell with a 3d^2 configuration have generated a tremendous amount of interest in recent years [1–8] with research covering V^{3+}, Cr^{4+} and Mn^{5+} doped into both single crystals and glasses. This is largely due to the observation of lasing in tetravalent chromium doped forsterite (Mg$_2$SiO$_4$) [9–11] and yttrium aluminium garnet (Y$_3$Al$_5$O$_{12}$, YAG) [12, 13], and thus the promise of future materials for the manufacture of near-infrared laser devices. Naturally, tetravalent chromium-doped materials have been most extensively investigated from yttrium oxyorthosilicate (Y$_2$SiO$_5$) [14] to forsterite [9], YAG [12], LiAlO$_2$ [15] and Ca$_2$GeO$_4$ [2]. Forty-three femtosecond pulses have recently been generated from an all solid state YAG:Cr^{4+} laser [16]. However, infrared emitters suffer (to varying degrees) from the effects of non-radiative multiphonon relaxation, which annihilates the optical excitation necessary for laser action. This is especially problematic as most real devices are designed to operate at room temperature, where these effects are

[4] Author to whom any correspondence should be addressed.

pronounced due to stimulated phonon emission. This represents a major problem, as lattice dynamics are not easily 'engineered' in the same way that static effects such as crystal-field splittings may be.

This work presents pump–probe measurements of non-radiative relaxation for V^{3+}-doped $LiAlO_2$ crystals. In particular, the relaxation of the $^3T_1$ electronic state through internal conversion has been measured and the energy barrier for such processes to occur has been determined. In this material, the vanadium replaces the slightly smaller Al^{3+} ions on a tetrahedral (T_d) symmetry site and thereby enters the crystal in the trivalent state, having a $3d^2$ configuration. Much of the early work on tetrahedrally coordinated V^{3+} has focused on III–V semiconducting compounds [17, 18]. The impetus for the semiconductor work has been largely motivated by the search for thermally stable dopants that give deep acceptor levels close to the intergap separation and thus provide materials that act as semi-insulating substrates. A range of V^{3+}-doped oxide crystals has been investigated recently, including YAG [19, 20], $LiAlO_2$, $LiGaO_2$, and $SrAl_2O_4$ [21, 22]. In these studies, it was found that emission of the V^{3+} was strongly quenched by non-radiative relaxation and the system is characterized by extremely low radiative quantum efficiency at less than 1%. Relatively few studies have reported ultrafast measurements of non-radiative relaxation (via, for example, a pump–probe measurement). A notable exception is the work of Alfano's group on Cr^{3+} and Cr^{4+} [23–25]. An excellent overview of transition-series-ion-doped laser gain media is given in [26].

2. Experimental considerations

The crystals used in this study were grown by the top-seeded solution-growth technique in the Optical Materials Research Centre at the University of Strathclyde, Glasgow. The samples were cut to yield a sample thickness of 2 mm and were polished to provide a good quality optical finish, thus minimizing the effects of scatter at the sample surfaces. Preliminary optical characterization was performed with an AVIV Associates 14DS double-beam spectrophotometer with crystals cooled to a base temperature of 10 K using a Leybold cryogenic refrigeration unit.

Time-resolved experiments have been performed with a Coherent Ti:sapphire-based ultrafast laser system consisting of a Mira 900-F oscillator and a RegA-900 regenerative amplifier. The RegA produces 120–150 fs FWHM 800 nm laser pulses at a repetition rate variable between 100 and 300 kHz. The energy per pulse is typically 4 μJ at a repetition rate of 300 kHz. For the experiment, the output from the regenerative amplifier was split 95:5 into a pump and a probe pulse, both of which were linearly polarized along the same axis. The probe pulse was optically delayed using a 0.1 μm step size motorized delay stage. Both laser 'beams' were focused onto the sample with two separate 15 cm focal length CaF_2 lenses and spatially overlapped. The focused spot size was less than 100 μm in diameter. The pump and probe pulses were temporally overlapped using second-harmonic generation in a beta barium borate crystal (BBO) in an autocorrelation type arrangement. After transmission through the sample (cooled to 10 K in a Janis Supertran flow cryostat), the probe beam was detected using a silicon PIN photodiode. Lock-in detection was provided using a Stanford Research Systems model SRS 400 lock-in amplifier for modulation of the pump beam at 2 kHz.

3. Results and analysis

3.1. The energy levels of a $3d^2$ configuration ion under T_d and C_2 symmetry

Under the influence of a tetrahedral (T_d) symmetry crystal-field potential, the ^3F Coulombic term of the $3d^2$ configuration (appropriate for trivalent vanadium and tetravalent chromium)
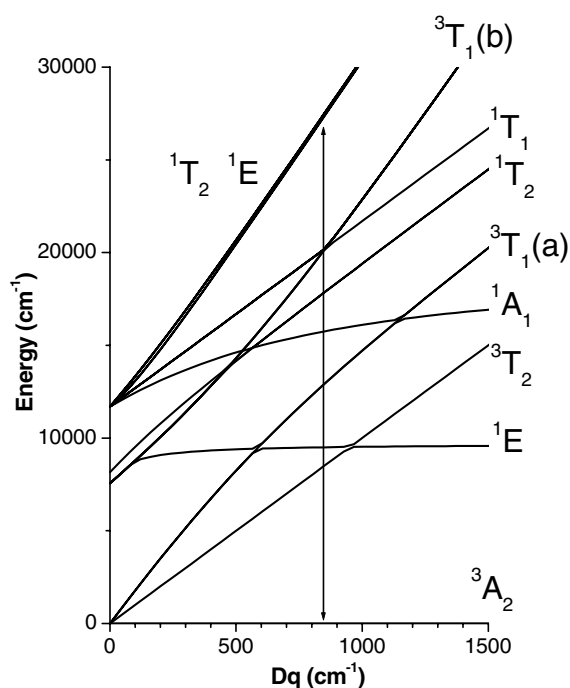
Figure 1. Tanabe–Sugano diagram for tetrahedrally coordinated 3d^2 configuration ions reproduced using values for the Racah parameters of $B = 504$ cm^{-1} and $C = 2822$ cm^{-1} from [21, 22]. The arrow corresponds to $Dq = 862$ cm^{-1} for V^{3+} in LiAlO$_2$.

splits into three spin triplet states: ^{3}A$_2$, ^{3}T$_2$ and ^{3}T$_1$ in order of increasing energy. An additional level ^{1}E, which is derived from the ^{1}D term, is essentially static in energy with respect to increasing crystal-field strength, lying close to 9500 cm^{-1} for LiAlO$_2$:V^{3+} [21, 22] and in between the ^{3}T$_2$ and ^{3}T$_1$ states. In figure 1 the Tanabe–Sugano diagram [27] of the V^{3+} (3d^2) system in a tetrahedral field is presented. The energies are determined by the Racah parameters B and C and crystal field strength Dq. The ^{3}A$_2$ ground state is independent of the magnitude of the crystal field. The first excited state can be either ^{3}T$_2$ for weak crystal fields or ^{1}E for the strong-crystal-field case. The vertical line in figure 1 denotes the energy level structure for LiAlO$_2$:V^{3+} that has been reproduced using values for the Racah parameters of $B = 504$ cm^{-1}, $C = 2822$ cm^{-1} and $Dq = 862$ cm^{-1} from Kück and Jander [21, 22]. In fact, an accurate description of the crystal field for the V^{3+} site has C$_2$ point group symmetry. This causes an additional splitting of the ^{3}T$_2$ and ^{3}T$_1$ states into three components, A, B and B [28], labelled by their C$_2$ irreducible representations. For further consideration of non-radiative transitions we have used the energies of the lowest components (the A components) for the energies of the ^{3}T$_2$ and ^{3}T$_1$ states (at 7450 and 10 420 cm^{-1} respectively).

3.2. Pump–probe results

The wavelength degenerate pump–probe experiments were performed by exciting directly into the vibronically broadened ^{3}T$_1$ states near 12 500 cm^{-1} using pump–pulse energies of around 1 μJ. Figure 2 shows the recorded pump–probe signals at temperatures of 4, 80, and 300 K. The measured decay traces are single exponential to within the accuracy of the data, having a 4 K decay time τ_{nr} (4 K) of 199 ps. The sharp feature observed around $t = 0$ is associated with
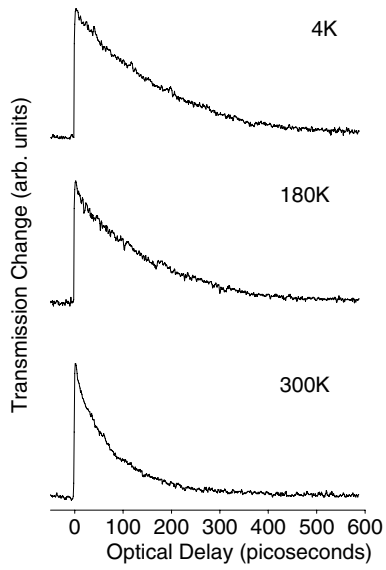
Figure 2. Pump–probe signals for $LiAlO_2:V^{3+}$ measured at $\lambda = 800$ nm for sample temperatures of 4, 180 and 300 K.

pump-beam diffraction into the probe-beam path, giving rise to the so-called 'coherent artifact', and will be neglected henceforth. The measured decay rate ($\Gamma_{nr} = 1/\tau_{nr}$) is found to increase by a factor of approximately 2.5 between 4 and 300 K. The fact that the measured decay times are around the picosecond timescale provides strong evidence that we are measuring the non-radiative decay of the $^3T_1$ state, since the intrinsic radiative lifetimes would be expected to be of the order of hundreds of microseconds. Furthermore, no luminescence is observed or expected from this manifold [21, 22].

3.3. Non-radiative processes in $LiAlO_2:V^{3+}$

To model the non-radiative processes in $LiAlO_3:V^{3+}$, we have to take into account the coupling of the d electrons with the lattice. The ground state $^3A_2$ and the excited ^1E state belong to the ground e^2 electronic configuration, whereas the exited states $^3T_2$ and $^3T_1$ belong to the excited electronic configurations $e^1t_2^1$, $e^1t_2^1$ and t_2^2, respectively (the second excited state is a mixture of the $e^1t_2^1$ and t_2^2 electronic configurations). In the one-electron approximation, excitation into the $^3T_2$ and $^3T_1$ states is equivalent to a transition of one electron from the e to t_2 orbital. The lattice relaxation that takes place does so as a response to the new shape of the electron cloud. The electron–lattice interaction is taken into account as an addition to the crystal-field Hamiltonian with two terms describing lattice vibration and electron–lattice coupling, and we obtain

$$H(Q) = H_0 + \tfrac{1}{2}k \cdot (Q - Q_0)^2 + V \cdot (Q - Q_0). \tag{1}$$

In equation (1), H_0 is the purely electronic Hamiltonian that is represented by crystal-field and Racah parameters. The coefficient labelled k is the elastic constant of the system and V describes the interactions of the electrons in the ground and excited configurations with the lattice. Q is the configurational coordinate and Q_0 is a constant representing the equilibrium value of the configurational coordinate. When the symmetrical 'breathing' vibrational mode is considered, all of the Q-dependent parts of the Hamiltonian contribute only through their diagonal matrix elements (the off-diagonal elements of the electron–lattice coupling are equal to zero).
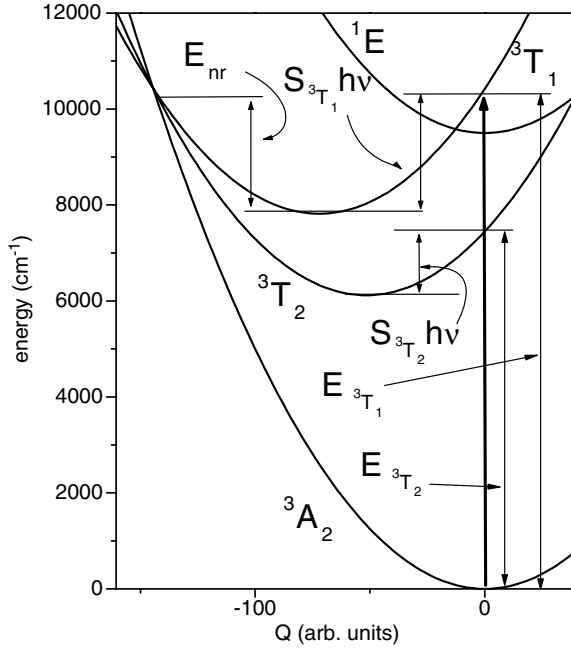
Figure 3. Configurational coordinate diagram for LiAlO$_2$:V^{3+} (see text for details). The bold arrow shows the Frank–Condon absorption transition.

In the crystal-field approximation, the potential V can be calculated as follows:

$$V = \left\langle \varphi \Big| \frac{dU_{cr}(Q)}{dQ} \Big| \varphi \right\rangle \approx \frac{d}{dQ} \langle \varphi | U_{cr} | \varphi \rangle, \tag{2}$$

where φ is the electronic wavefunction and $\langle \varphi | U_{cr} | \varphi \rangle = \frac{C}{Q^5}$ is the crystal-field potential. One can choose the origin of the configurational coordinate at a point corresponding to the minimum energy of the ground electronic manifold $^3A_2$. The crystal-field Hamiltonian is different in different electronic configurations. One defines $V_{e^2} = 0$ and $V_{t_2^2} = 2 \cdot V_{e^1t_2^1}$ and the energy of the lattice or electron–lattice relaxation for the jth state belonging to the ith electronic configuration is given by

$$S_{j(i)}\hbar\omega = \frac{V_i^2}{2k}, \tag{3}$$

where $S_{j(i)}$ is the Huang–Rhys factor and $\hbar\omega$ is the phonon energy. Equation (3) is valid for the $^3T_2$ state, which is formed by electrons from the excited $e^1t_2^1$ electronic configuration. In the case of $^3T_1$, which is formed by a superposition of the $e^1t_2^1$ and t_2^2 electronic configurations, the final electron–lattice coupling energy is $\frac{V_{e^1t_2^1}^2}{2k} < S_{^3T_1}\hbar\omega \leqslant \frac{V_{t_2^2}^2}{2k}$. In figure 3 the energies of the lowest states of V^{3+} are presented in the form of a configurational coordinate diagram. One sees that each electronic manifold is represented by a parabola, which depicts the vibronic energy. The minimum energy of the $^3A_2$ and ^1E electronic manifolds appear at the same value of Q. The parabolas representing the $^3T_2$ and $^3T_1$ states are shifted in configurational space. To parametrize the diagram we have used an energy of the ^1E state determined by the values for the Racah parameters as well as energies of the lowest components of the $^3T_2$ and $^3T_1$ states obtained from experiment ($^3T_1$) and partly from calculations including the C_2 symmetry field ($^3T_2$). Explicitly, our values are obtained as a difference between the average value of the calculated energy of the lowest component of the $^3T_2$ state (7030 cm^{-1} according to [28] and 7886 cm^{-1} according to [22], yielding 7450 cm^{-1}) and the experimental energy

of the zero-phonon $^3T_2 \rightarrow {}^3A_2$ transition (6120 cm^{-1}, [21]). Thus we have assumed that $S_{^3T_2}\hbar\omega = 1330$ cm^{-1}, which is greater than the value of 925 cm^{-1} suggested by Kück and Jander [21]. One can see in figure 3 that the potential curves corresponding to the $^3A_2$, $^3T_2$ and $^3T_1$ electronic manifolds cross over at the same point. This is not an accident and is related to our assumptions for the crystal-field U_{cr} and electron–lattice coupling. According to the strong crystal-field model, the energies of the excited states with respect to the ground state satisfy the relation $E_{^3T_1} = \langle\varphi_{^3T_1}|U_{cr}|\varphi_{^3T_1}\rangle = 2E_{^2T_2} = 2 \cdot \langle\varphi_{^3T_2}|U_{cr}|\varphi_{^3T_2}\rangle$ and $V_{^3T_1} = 2 \cdot V_{^3T_2}$. Thus the $^3A_2$–$^3T_2$ and $^3A_2$–$^3T_1$ crossing takes place at the same point of configurational space, $Q_{cr} = \frac{\langle\varphi_{^3T_2}|U_{cr}|\varphi_{^3T_2}\rangle}{V_{^3T_2}}$. Considering equation (1), it is seen that such a cross-over takes place at the same point of configurational space when the relations $E_{^3A_2} = 0$, $V_{^3A_2} = 0$ and $\frac{E_{^3T_2}}{V_{^3T_2}} = \frac{E_{^3T_{1(a)}}}{V_{^3T_{1(a)}}}$ are satisfied and independent of their relationship to the crystal field. In our case, the first two relations are valid whilst the third relationship is approximately so. In our calculations, we have used $E_{^3T_2} = 7450$ cm^{-1} $E_{^3T_{1(a)}} = 10\,420$ cm^{-1} (the experimental value, [21]), and $V_{^3T_{1(a)}} = V_{^3T_2}\frac{E_{^3T_{1(a)}}}{E_{^3T_2}}$. Thus a single crossing of the $^3A_2$, $^3T_2$ and $^3T_1$ electronic manifolds in configurational space results from the assumption that $\frac{E_{^3T_2}}{V_{^3T_2}} = \frac{E_{^3T_{1(a)}}}{V_{^3T_{1(a)}}}$. Actually, if $\frac{E_{^3T_2}}{V_{^3T_2}} < \frac{E_{^3T_{1(a)}}}{V_{^3T_{1(a)}}}$ the $^3T_2$–$^3A_2$ crossover takes place for a lower energy than $^3T_1$–$^3A_2$, which in turn has a lower energy than $^3T_1$–$^3T_2$. If $\frac{E_{^3T_2}}{V_{^3T_2}} > \frac{E_{^3T_{1(a)}}}{V_{^3T_{1(a)}}}$ the sequence is reversed. In figure 3, the energy barrier for the non-radiative internal conversion process that depopulates the $^3T_1$ state is equal to ~ 2000 cm^{-1} as a result of the relatively large electron–lattice coupling. It is this fact that causes the strong temperature dependence of the decay times measured in our pump–probe experiments.

To account for the temperature dependent lifetimes, we have considered non-radiative processes in the vibronic states of the $^3T_1$ electronic manifold. In thermal equilibrium one can calculate the non-radiative lifetime using the following formula [29–31]:

$$\tau_{nr}(T) = \frac{\sum_{n=0} \exp\left[-\frac{E_{^3T_1}^n - E_{^3T_1}^0}{kT}\right]}{\sum_{n=0} W_n \exp\left[-\frac{E_{^3T_1}^n - E_{^3T_1}^0}{kT}\right]} \tag{4}$$

where $E_{^3T_1}^n = (n + \frac{1}{2})\hbar\omega$ and is associated with the nth vibronic state of the $^3T_1$ electronic manifold and W_n is the non-radiative rate describing the depopulation of this state. The main reason for the non-radiative depopulation is non-radiative internal conversion where an electron jumps from the $^3T_1$ electronic manifold directly to a highly excited vibronic state of the ground electronic manifold $^3A_1$. Thus one can define [31]

$$W_n = \frac{2\pi}{\hbar}|T_{^3T_1{}^3A_2}|^2 \cdot |\langle\chi_{^3T_1}^n|\chi_{^3A_2}^m\rangle|^2\delta\left[E_{^3T_1}^n - E_{^3A_1}^m\right] \tag{5}$$

where $T_{^3T_1{}^3A_2}$ is the electronic transition moment that mixes the $^3T_1$ and $^3A_1$ states, $\langle\chi_{^3T_1}^n\chi_{^3A_2}^m\rangle$ is the overlap integral of the respective vibronic wavefunctions and δ is a Dirac function that selects the energies of the vibronic states. For the case when the energy barrier E_{nr} is comparable to the phonon energy, one can replace relation (4) by Mott's formula [32]:

$$\tau_{nr}(T) = \frac{1}{W_0 + W_1 \exp[\frac{-E_{nr}}{kT}]}, \tag{6}$$

where W_0 is the rate of non-radiative depopulation of the zero-phonon level of the $^3T_1$ state (and can be considered as the probability of tunnelling through the potential barrier) and W_1 is the rate of phonon assisted barrier hopping, where E_{nr} is the barrier height and k is
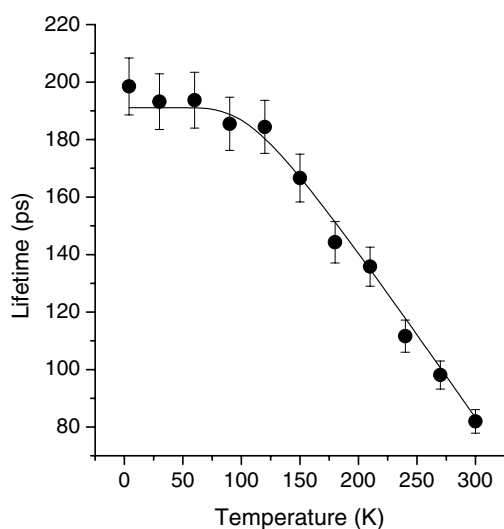
Figure 4. Temperature-dependent decay times for the $^3T_1$ state in LiAlO$_2$:V^{3+} after pulsed excitation at 800 nm. The solid line is a fit to equation (6) in the text using parameters $W_0 = (5.2 \pm 1) \times 10^9$ Hz, $W_1 = (7.5 \pm 1) \times 10^{10}$ Hz and $E_{nr} = 530 \pm 50$ cm^{-1}.

Boltzmann's constant. The result of fitting equation (6) to our experimental data is presented as a solid curve in figure 4. The best fit has been obtained for $W_0 = (5.2 \pm 1) \times 10^9$ Hz, $W_1 = (7.5 \pm 1) \times 10^{10}$ Hz and $E_{nr} = 530 \pm 50$ cm^{-1}. The relatively small value of W_1 (it is expected that $|T_{^3T_1 ^3A_2}|^2$ should be of the order of 10^{13} Hz [29]) and the energy barrier E_{nr} (from the configurational coordinate diagram in figure 3, a value of $E_{nr} = 1000$ cm^{-1} might be expected) is related to the fact that we deal with tunnelling through the barrier from higher excited vibronic states of the $^3T_1$(a) electronic manifold and therefore W_1 is diminished by the quantity $|\langle \chi^1_{^3T_1} | \chi^m_{^3A_2} \rangle|^2$.

We have omitted the depopulation pathway of the $^3T_1$ state, which involves a non-radiative transfer $^3T_1$ to $^3T_2$, non-radiative relaxation inside the $^3T_2$ manifold and radiative processes from $^3T_2$ to $^3A_2$. Actually, since the repopulation of the $^3A_2$ state takes place on a timescale of the order of 100 ps and the radiative $^3T_2 \rightarrow {}^3A_2$ lifetime should be of the order of 10–100 μs, any $^3T_2 \rightarrow {}^3A_2$ emission will be extremely weak, if present at all. From a theoretical point of view the $^3T_2 \rightarrow {}^3A_2$ emission is negligible if the condition $\frac{E_{^3T_2}}{V_{^3T_2}} \leqslant \frac{E_{^3T_{1(a)}}}{V_{^3T_{1(a)}}}$ is satisfied. Then, as has been mentioned, the energy of the $^3A_2$–$^3T_2$ crossover is lower than or equal to the energy of $^3A_2$–$^3T_1$. Thus after excitation to the $^3T_1$ state the first non-radiative process is the $^3T_1 \rightarrow {}^3A_2$ transition; next, the system reaches the $^3A_2$–$^3T_2$ crossover due to relaxation in the $^3A_2$ electronic manifold. The probability that the system (after leaving the $^3A_2$–$^3T_2$ crossover) 'localizes' at $^3A_2$ or $^3T_2$ is proportional to the relative energy of the crossover with respect to the minimum energy of the respective electronic manifold [30]. Since this energy is much greater for the $^3A_2$ electronic manifold, the population of the $^3T_2$ state is small. Conversely, when $\frac{E_{^3T_2}}{V_{^3T_2}} > \frac{E_{^3T_{1(a)}}}{V_{^3T_{1(a)}}}$ the $^3T_1$–$^3T_2$ crossover occurs at a lower energy than $^3A_2$–$^3T_2$. In this case the first step in the depopulation of $^3T_1$ is the $^3T_1 \rightarrow {}^3T_2$ non-radiative transition. Then non-radiative relaxation within the $^3T_2$ electronic manifold and a radiative $^3T_2 \rightarrow {}^3A_2$ transition is more probable than depopulation of $^3T_2$ due to non-radiative $^3T_2 \rightarrow {}^3A_2$ processes.

4. Conclusions

We have measured non-radiative internal conversion from the $^3T_1$ manifold to the $^3A_2$ ground state in LiAlO$_2$ doped with trivalent vanadium using a wavelength degenerate pump–probe

technique. The $^3T_1$ decay time has been measured to be 199 ps at 4 K, decreasing to a value of 82 ps at room temperature. Using Mott's expression, we have determined the relative probabilities for non-radiative phonon-assisted barrier hopping and quantum mechanical tunnelling through the potential barrier to the $^3A_2$ ground state, yielding best fit parameters of $W_0 = (5.2 \pm 1) \times 10^9$ Hz and $W_1 = (7.5 \pm 1) \times 10^{10}$ Hz for a potential barrier of $E_{nr} = 530 \pm 50$ cm^{-1}.

Acknowledgments

References

[1] Jia W, Lu L, Tissue B M and Yen W M 1991 *J. Cryst. Growth* **109** 329
[2] Hazenkamp M F, Gudel H U, Atanasov M, Kesper U and Reinen D 1996 *Phys. Rev.* B **53** 2367
[3] Scott M A, Russell D L, Henderson B, Han T P J and Gallagher H G 1998 *J. Cryst. Growth* **183** 366
[4] Kück S, Petermann K, Pohlmann U and Huber G 1996 *J. Lumin.* **68** 1
[5] Scott M A, Henderson B, Gallagher H G and Han T P J 1997 *J. Phys.: Condens. Matter* **9** 9893
[6] Jousseaume C, Vivien D, Kahn-Harari A and Malkin B Z 2003 *Opt. Mater.* **24** 143
[7] Sharonov M Yu, Bykov A B, Owen S, Petricevic V and Alfano R R 2003 *J. Appl. Phys.* **93** 1044
[8] Malyarevich A M, Volk Yu V, Yumashev K V, Pavlovskii V K, Zapalova S S, Dymshits O S and Zhilin A A 2005 *J. Non-Cryst. Solids* **351** 3551
[9] Guyot Y, Manaa H, Moncorge R, Garnier N, Descroix E and Larporte P 1994 *J. Physique Coll.* **4** 529
[10] Petricevic V, Gayen S K and Alfano R R 1988 *Appl. Phys. Lett.* **53** 2590
[11] Verdun H R, Thomas L M, Andrauskas D M, McCollum T and Pinto A 1988 *Appl. Phys. Lett.* **53** 2593
[12] Shkadarevich A P 1989 *OSA Proc. on Tunable Solid State Lasers* vol 5, ed M L Shand and M P Jenssen (North Falmouth: Optical Society of America) p 60
[13] Zverew G M and Shestakow A V 1989 *OSA Proc. on Tunable Solid State Lasers* vol 5, ed M L Shand and M P Jenssen (North Falmouth: Optical Society of America) p 66
[14] Koetke J, Kück S, Petermann K, Huber G, Cerullo G, Danilov M, Magni V, Qian L F and Svelta O 1993 *Opt. Commun.* **101** 195
[15] Kück S, Hartung S, Petermann K and Huber G 1995 *Appl. Phys.* B **61** 33
[16] Tong Y P, French P M W, Taylor J R and Fujimoto J O 1997 *Opt. Commun.* **13** 235
[17] Clerjaud B 1985 *J. Phys. C: Solid State Phys.* **18** 3615
[18] Schulz H J and Thiede M 1988 *J. Phys. C: Solid State Phys.* **21** L1033
[19] Weber M J and Riseberg L A 1971 *J. Chem. Phys.* **55** 2032
[20] Mikhailov V P, Kuleshov N V, Zhavoronkov N I, Prokoshin P V and Yumashev K V 1993 *Opt. Mater.* **2** 267
[21] Kück S and Jander P 1999 *Chem. Phys. Lett.* **300** 189
[22] Kück S and Jander P 1999 *Opt. Mater.* **13** 299
[23] Gayen S K, Wang W B, Petricevic V and Alfano R R 1986 *Appl. Phys. Lett.* **49** 437
[24] Demos S G, Calistru D M and Alfano R R 1996 *Appl. Phys. Lett.* **68** 1195
[25] Calistru D M, Demos S G and Alfano R R 1997 *Phys. Rev. Lett.* **78** 374
[26] Kück S 2001 *Appl. Phys.* B **72** 515
[27] Sugano S, Tanabe Y and Kamimura H 1970 *Multiplers of Transition Metal Ions in Crystals* (New York: Academic)
[28] Kammoun S 2002 *Phys. Status Solidi* b **232** 306
[29] Struck C W and Fonger W H 1975 *J. Lumin.* **10** 1
[30] Grinberg M and Mandelis A 1994 *Phys. Rev.* B **49** 12496
[31] Grinberg M and Jaskólski W 1997 *Phys. Rev.* B **55** 5581
[32] Mott N F 1938 *Proc. R. Soc.* A **176** 384